Mon. Not. R. Astron. Soc. **000**, 000–000 (0000) Printed 19 June 2017 (MN LATEX style file v2.2)

A multi-wavelength study of SXP 1062, the long period X-ray pulsar associated with a supernova remnant

A. González-Galán[1], L. M. Oskinova[1⋆], S. B. Popov[2], F. Haberl[3], M. Kühnel[4], J. Gallagher III[5], M. P. E. Schurch[6], M. A. Guerrero[7]

[1] *Institute for Physics and Astronomy, University of Potsdam, D-14476 Potsdam, Germany*
[2] *Sternberg Astronomical Institute, Lomonosov Moscow State University, 119992 Moscow, Russia*
[3] *Max-Planck-Institut für extraterrestrische Physik, Giessenbachstraße, 85748 Garching, Germany*
[4] *Dr. Karl Remeis-Sternwarte & ECAP, Universität Erlangen-Nürnberg, Sternwartstr. 7, 96049 Bamberg, Germany*
[5] *University of Wisconsin-Madison, 475 N. Charter St. Madison, WI 53706 USA*
[6] *Astrophysics, Cosmology and Gravity Centre (ACGC), Astronomy Department, University of Cape Town, Rondebosch, Private Bag X1 7701, South Africa*
[7] *Instituto de Astrofísica de Andalucía, IAA-CSIC, Glorieta de la Astronomía s/n, 18008 Granada, Spain*

19 June 2017

ABSTRACT

SXP 1062 is a Be X-ray binary located in the Small Magellanic Cloud. It hosts a long-period X-ray pulsar and is likely associated with the supernova remnant MCSNR J0127-7332. In this work we present a multi-wavelength view on SXP 1062 in different luminosity regimes. The data set analyzed in this paper consists of optical *OGLE* photometric data, an X-ray monitoring campaign with *Swift*, *XMM-Newton* observations during quiescence of the source, *Chandra* observations following an X-ray outburst, as well as optical spectroscopy using the RSS/*SALT* telescope obtained nearly simultaneously with the *Chandra* observations. During this campaign we observed a tight coincidence of an X-ray and an optical outburst, i.e., a typical Type I outburst as often detected in Be X-ray binaries at periastron passage of the neutron star. To explain the results of our multi-wavelength campaign we propose a simple scenario where the disc of the Be star is observed face-on, while the orbit of the neutron star is inclined with respect to the disc. According to the model of quasi-spherical settling accretion our estimation of the magnetic field of the pulsar in SXP 1062 does not require an extremely strong magnetic field at the present time.

Key words: pulsars: individual: SXP 1062 - galaxies: individual: Small Magellanic Cloud - stars:neutron - X-rays: binaries

1 INTRODUCTION

Be X-ray binaries (BeXBs; Reig 2011) are a subgroup of high mass X-ray binaries. The donor stars in these interesting objects are non-supergiant, fast-rotating B-type stars with decretion discs. The compact objects, in most confirmed BeXBs, are magnetized rotating neutron stars (NSs). Therefore, the majority of BeXBs are X-ray pulsars (Nagase 1989). The accretion in BeXBs is likely powered by the interaction between the decretion disc of the Be star and the NS (Okazaki & Negueruela 2001).

The subject of this study, SXP 1062, is an X-ray pulsar located in the Wing of the Small Magellanic Cloud (SMC) discovered by *Chandra* and *XMM-Newton* in March 2010 (Hénault-Brunet et al. 2012; Haberl et al. 2012). The optical counterpart of SXP 1062 is the Be star 2dFS 3831 (B0-0.5III; Evans et al. 2004). From the analysis of these first observations a long X-ray pulse period $P_{\rm spin} \sim 1062$ s was found.

SXP 1062 is especially interesting because it is the first X-ray pulsar most likely residing in its parental supernova remnant (SNR). The association of SXP 1062 with MCSNR J0127-7332[1] allows to estimate the age of the NS. Two independent groups obtained compatible values for the kinematic age of MCSNR J0127-7332 of $\sim 2-4\times10^4$ years (Hénault-Brunet et al. 2012), and $\sim 1.6\times10^4$ years (Haberl et al. 2012).

⋆ E-mail: lida@astro.physik.uni-potsdam.de

[1] `http://sci.esa.int/xmm-newton/49789`

Table 1. Log of X-ray *Chandra* and *XMM-Newton* observations. There are five different observations as indicated in the first column.

#	Instrument	ObsID	MJD	Date	Exp Time (ks)	ΔE (keV)
1	EPIC-MOS1/*XMM-Newton*	0721960101	56606.79	2013-10-11	77.1	0.2 − 10
1	EPIC-MOS2/*XMM-Newton*	0721960101	56606.79	2013-10-11	77.2	0.2 − 10
1	EPIC-pn/*XMM-Newton*	0721960101	56606.80	2013-10-11	66.2	0.2 − 15
2	ACIS/*Chandra*	15784	56827.80	2014-06-19	29.6	0.3 − 10
3	ACIS/*Chandra*	15785	56837.49	2014-06-29	26.8	0.3 − 10
4	ACIS/*Chandra*	15786	56846.30	2014-07-08	26.3	0.3 − 10
5	ACIS/*Chandra*	15787	56856.91	2014-07-18	25.0	0.3 − 10

NOTE: The exposure time is the sum of good time intervals after removing times of high background.

According to standard models, at this age the NSs are too young to be in the accretor phase, and, consequently, are not expected to be X-ray pulsars (Lipunov 1992, and references therein).

A number of models and scenarios are suggested to explain the physics of SXP 1062. Haberl et al. (2012) proposed that its NS was born with unusually long initial spin period significantly larger than 0.1 s. Popov & Turolla (2012) suggested that the NS is spinning close to the equilibrium period and has a current magnetic field of $B \lesssim 10^{13}$ G at present time, while initially it had a strong magnetic field in excess of $B \sim 10^{14}$ G. Ikhsanov (2012) put forward a magnetic accretion scenario, while Fu & Li (2012) explored the possibility that SXP 1062 is a present day accreting magnetar.

In this paper we use a complex multi-wavelength approach and analyse a large set of data with the goal to shed new light on the origin and properties of SXP 1062. The data were collected during the quiescent stage as well as at outburst. The optical observations were obtained with the *SALT* telescope; we also use publicly available OGLE data. The X-ray observations analysed in this paper are obtained with *Swift* (long time monitoring), *XMM-Newton* (in quiescence) and *Chandra* (in outburst). The optical and X-ray observations were coordinated during outburst. The paper is organized as follows. Section 2 presents the new data and observations. Section 3 is dedicated to the data analysis and results. In Section 4 we compare our results with previous results and discuss the enigmatic properties of SXP 1062. Finally, in Section 5 we present a summary and our final conclusions.

2 OBSERVATIONS

2.1 X-ray data

2.1.1 EPIC/XMM-Newton

The European Photon Imaging Camera (EPIC; **?**Strüder et al. 2001), on board of the *XMM-Newton* observatory comprises a set of three X-ray CCD cameras: EPIC-MOS1, EPIC-MOS2, and EPIC-pn. The EPIC-pn covers an energy range between 0.2 and 15 keV, while the EPIC-MOS1 and EPIC-MOS2 are sensitive at energies between 0.2 and 10 keV.

We obtained an *XMM-Newton* observation with the EPIC instruments in full-frame mode (Table 1) during quiescence of SXP 1062 (pink vertical line in the bottom panel of Fig. 1). The *XMM-Newton* data were reduced with the Science Analysis Software (XMMSAS, version 13.5).

2.1.2 XRT/Swift

The X-ray Telescope (XRT) mounted on the *Swift* observatory (**?**) operates in the energy range 0.3 − 10 keV. XRT was monitoring SXP 1062 between 2012-10-09 and 2014-10-26 (TargetID: 91 814, see bottom panel in Fig. 1). During this monitoring campaign an X-ray outburst was detected on 2014-06-01 (ObsID: 00091814001). The detection of the X-ray outburst triggered our target of opportunity *Chandra* observing campaign.

2.1.3 ACIS/Chandra

The *Chandra* Advanced CCD Imaging Spectrometer (ACIS; Garmire 2001), on board *Chandra* is sensitive in the 0.3 − 10 keV energy range. We obtained four *Chandra* observations (see Table 1) triggered by the outburst detected during our XRT/*Swift* monitoring campaign (times of observations are marked in Fig. 1 as green vertical lines). Our optical RSS/*SALT* observations (see Section 2.2.1) were accumulated nearly simultaneously. The first *Chandra* observation was performed using the *Continuous Clocking Mode* which is recommended for very bright sources as it prevents the photon pile-up. The other three exposures were obtained with the standard *Timed* read out mode. The *Chandra* data were reduced with version 4.6 of the Chandra Interactive Analysis of Observations (CIAO) software.

2.2 Optical data

2.2.1 RSS/SALT

The optical spectroscopy was collected using the Robert Stobie dual-beam Visible/Near-IR spectrograph mounted on the *SALT* 11 m telescope (RSS; Kobulnicky et al. 2003).

We obtained four sets of observations (see Table 2) which are part of the programs 2014-1-RSA_OTH-22 and 2016-2-RSA-044. Three data sets were obtained in 2014 after the outburst detected by our *Swift* monitoring campaign (observing times are indicated in the top-panel of Fig. 1 as red vertical lines) and are quasi-simultaneous with our *Chandra* observations. The data sets consist of long-slit spectra using two different long-slit set-ups. The first covers wavelengths between 6082 Å and 6925 Å, i.e., the Hα emission line, with a slit width of either 1.25″ (first observation) or 1.5″ (rest of observations). The second set-up covers the range between 3835 Å and 4924 Å, i.e., Hβ and Hγ emission lines with a slit width of 1.5″.

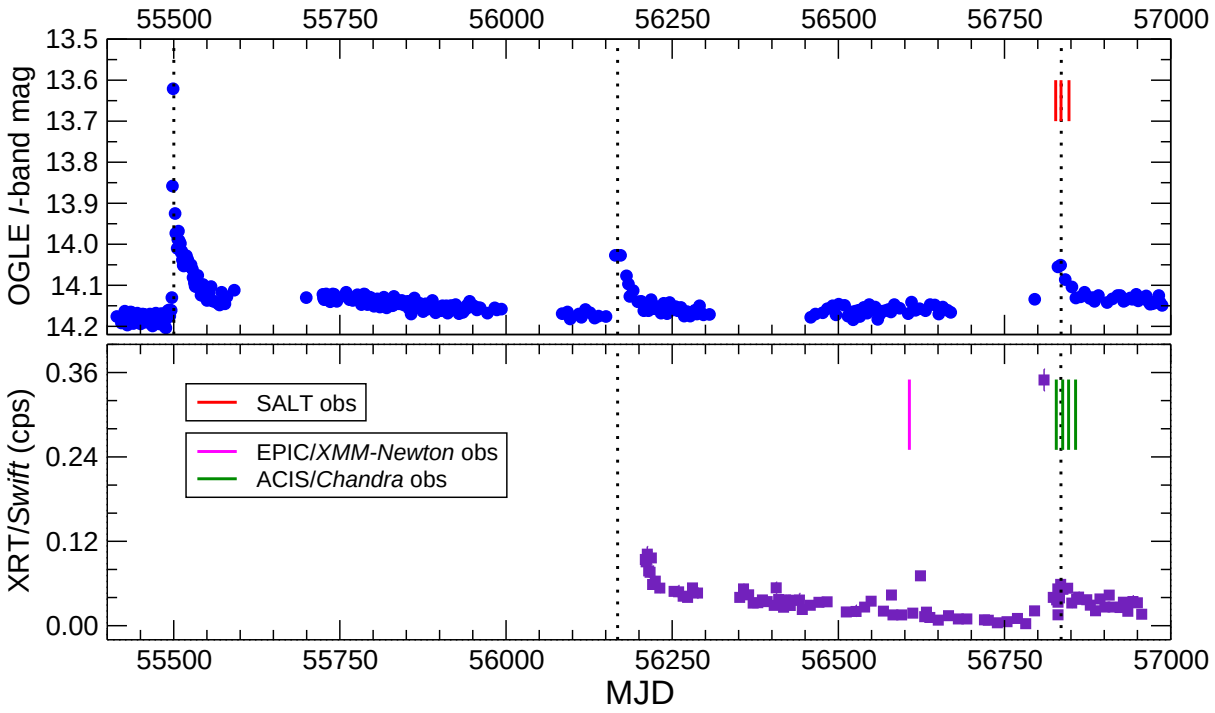

Figure 1. *Upper panel:* OGLE I-band light curve covering SXP 1062 between 2010-08-06 (MJD 55414.14) and 2014-11-26 (MJD 56987.10). The red vertical lines indicate the epochs of the optical RSS/*SALT* observations. *Bottom panel:* XRT/Swift 0.3 − 10 keV X-ray light curve between 2012-10-09 (MJD 56209.50) and 2014-06-22 (MJD 56830.43). The pink vertical line indicates the epoch of the EPIC observation, and the green vertical lines indicate the epochs of the ACIS observations. The dotted vertical lines shown in both panels indicate the periastron passage of NS according to our analysis (Section 3.1). Note the coincidence between the X-ray outburst shown in the bottom panel with the third optical outburst shown in the upper panel.

Table 2. Log of optical RSS/*SALT* observations obtained with the VPH PG2300 grating.

#	MJD	Date	$\Delta\lambda$ (Å)
1	56827.80	2014-06-20	6082 − 6925
2	56835.49	2014-06-27	6082 − 6925
2		2014-06-27	3835 − 4924
2		2014-06-27	3835 − 4924
3	56847.30	2014-07-09	6082 − 6925
3		2014-07-09	3835 − 4924
3		2014-07-09	3835 − 4924
4	57694	2016-11-02	6082 − 6925

NOTE: The wavelength coverage of the grating changes with the input angle. The spectra covering the Hα region (6082 − 6925Å) were obtained with the angle of 48.875°, while the spectra covering the Hβ and Hγ region (3835 − 4924Å) were obtained with the angle of 30.5°.

The data were first processed using the PySALT[2] package. Subsequent flat-fielding, background subtraction, wavelength calibration, and extraction of 1D spectra were performed with the Image Reduction and Analysis Facility (IRAF[3]). After wavelength calibration and extraction, the final spectra were red-shift corrected for the systemic velocity of the SMC (150 km s^{-1}).

[2] `http://pysalt.salt.ac.za`
[3] `http://iraf.noao.edu`

Table 3. Equivalent widths of the Hα line in the optical spectra of SXP 1062.

MJD	EW (Å) Hα	Reference
55494	-23 ± 1	Hénault-Brunet et al. (2012)
56214	-26.7 ± 0.1	Sturm et al. (2013)
56827	-36.3 ± 0.6	This work
56835	-34.0 ± 0.6	This work
56847	-34.1 ± 0.6	This work
57694	-33 ± 1	This work

The equivalent width (EW) calculated by fitting a double Gaussian model are shown in Table 3 together with the previously published values for comparison.
Figure 2 displays the observed Hγ, Hβ and Hα profiles for RSS/*SALT* post-outburst observations. The strong Hβ and Hα lines have non-split symmetric shape. The spectrum around the Hγ line is more noisy and the line structures apparent in some observed spectra are due to the noise.

2.2.2 OGLE

The Optical Gravitational Lensing Experiment (OGLE) Monitoring system provides optical I-band photometry of X-ray sources[4] located in the fields observed with roughly

[4] `http://ogle.astrouw.edu.pl/ogle4/xrom/xrom.html`

daily sampling by the OGLE-IV Survey (Udalski 2008). To date there are seven seasons of data available for SXP 1062 covering the time interval from MJD 55414.4 (2010-08-06) to MJD 57773.039 (2017-01-20).

3 DATA ANALYSIS & RESULTS

3.1 Determination of orbital period based on the optical and X-ray light curves

In general, Be stars show photometric variability on various time scales (Porter & Rivinius 2003). Stellar rotation and pulsations are held responsible for fast variability, while long-term variability on time scales of a year is typical for formation and dissipation of the disc (Jones et al. 2008). Reig & Fabregat (2015) point out that since the disc constitutes the main reservoir of matter available for accretion, a correlation between X-ray and optical emission should be expected and is indeed often observed. Albeit no detailed simulations predicting the optical and X-ray light curves exist yet, the coincidence between optical and X-ray variability indicates that the disc material powers the X-rays through accretion. Typically, transient BeXBs experience X-ray outbursts at regular periastron passages. The time intervals between outbursts are usually attributed to binary orbital periods (e.g., Okazaki & Negueruela 2001; Negueruela et al. 2001).

As can be seen in the upper panel in Fig. 1, SXP 1062 shows regular outbursts in the optical. Schmidtke et al. (2012) proposed that the time interval of 656 ± 2 d between the first two optical outbursts is the orbital period of SXP 1062. Sturm et al. (2013) noticed the fast rise exponential decay (FRED)-shaped profile (Bird et al. 2012) of these optical outbursts, which supports their orbital origin, i.e., the outbursts occur at periastron passage of the NS.

The current OGLE-IV *I*-band light curve covers more than 6 yr. Three equi-distant outbursts were observed confirming their periodic nature and allowing to better constrain the orbital period. Unfortunately, during the latest outburst predicted for 2016-04-26 (MJD 57504), there was a gap in the OGLE observations. Hence, the latest predicted outburst was not recorded.

To further tighten the orbital period, we selected the minimum magnitude detected in the optical OGLE *I*-band light curve as the mid-time for the outbursts. Unfortunately, the spacing of the OGLE observations is somewhat sparse (roughly once a day), therefore we cannot precisely determine the exact time of the start of the outbursts. To overcome this difficulty, we took the time interval between the data points immediately before and after the mid-time as the uncertainty (second column of Table 4). As a next step, we calculated the time intervals between the outbursts (third column of Table 4), and the weighted average of these time intervals. Finally, we derive the orbital period of SXP 1062 to $P_{\rm orb} \approx 668 \pm 10$ days. However, one shall be aware, that in the standard scenario of NS-Be disc interactions, the outbursts might happen twice per orbital period, if the orbit is sufficiently tight and its eccentricity is mild. In this case, the true orbital period may be twice as large as we derived. As can be seen in Figure 1, the X-ray outbursts from SXP 1062 are regular and happen nearly at the same time as the optical ones. During our *Swift* monitoring campaign we have detected an X-ray outburst in excellent agreement with the predictions. This gives further credibility to the scenario where X-ray and optical outbursts in SXP 1062 occur simultaneously at the periastron passage of the NS. Fig. 1 also suggests that the minimum optical magnitude of each outburst is apparently increasing with time, i.e. ΔI is decreasing. This could be either of physical origin or due to the sparse data sampling.

Table 4. Outburst history of SXP 1062.

Outburst	MJD	Δt (days)	ΔI (mag)
1	55500.09 ± 0.97		$\gtrsim 0.55$
2	56166 ± 14	666 ± 7	$\gtrsim 0.15$
3	56835.9 ± 4.5	670 ± 8	$\gtrsim 0.11$

NOTE: The first column indicates the outburst ordered by date, the second column the outburst time. The third column provides the time interval between outbursts and the fourth column the amplitude of the outburst.

3.2 X-ray spectrum in quiescence measured by EPIC/XMM-Newton

X-ray spectra during outburst and quiescence were obtained by *Chandra* and *XMM-Newton*, respectively (see section 2.1). The spectral analysis was performed using the X-ray spectral fitting package XSPEC (Arnaud 1996). All spectra were fitted using a model which includes three absorption components. The first component accounts for the absorption in the Milky Way with a fixed column density $6 \times 10^{20}\,{\rm cm}^{-2}$ and solar abundances (Wilms et al. 2000). The second component accounts for the local absorption in the SMC, and has a fixed column density $2 \times 10^{21}\,{\rm cm}^{-2}$ (Oskinova et al. 2013) and SMC abundances (0.2 times solar for elements heavier than He; Russell & Dopita 1992). The third component, also with SMC abundances, accounts for the absorption intrinsic to SXP 1062. We keep this absorption component as a free parameter during the spectral fitting procedure.

X-ray luminosities in the energy range 0.2-15 keV assuming a distance modulus to the SMC Wing of $DM = 18.7$ (Cignoni et al. 2009) as well as X-ray fluxes in various energy bands are given in Tables 7, A1, and A2.

We start by considering the X-ray spectra measured during the quiescence by *XMM-Newton* (see Fig. 3). As a first step we have simultaneously fitted all three EPIC spectra (pn, MOS1 and MOS2) with an absorbed power law. The model fit shows residuals in the soft part of the spectra. Therefore, as a next step we tried to refine the model adding a black-body component. This led to a statistical improvement of the fit. We also tested a combination of a power law and an optically thin thermal plasma component (APEC; Smith et al. 2001) with SMC abundances. However, including this component does not improve the fit. Finally, the best fit is obtained using a power law together with a black-body component, and the thermal plasma component. This best-fit model is shown in Fig. 3, and the corresponding parameters for the various models are given in Table 5. Similar X-ray spectral properties of SXP 1062 were previously derived by

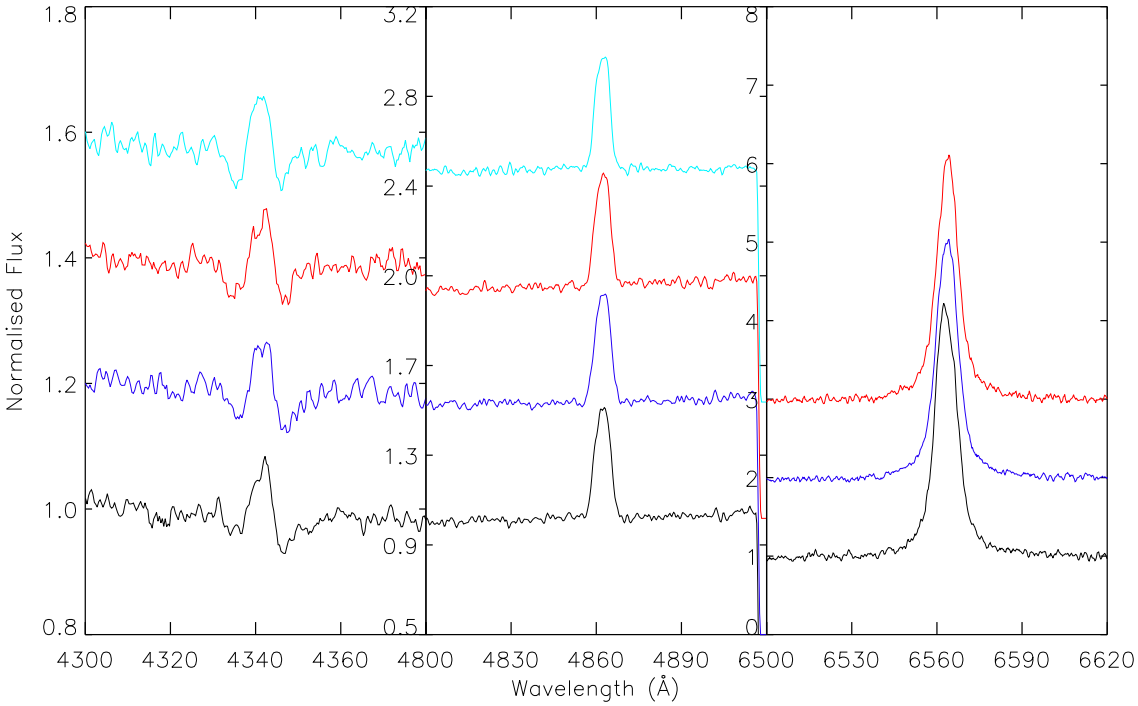

Figure 2. SXP 1062 Hγ (left), Hβ (middle) and Hα (right) profiles as observed during June 2014 after the outburst detected with *Swift*. Three different Hα profiles were obtained during three different nights, and four Hβ and Hγ profiles observed during two different nights (two spectra per night) as summarized in Table 2. The spectra displayed with an arbitrary offset for presentation purposes. The spectra are ordered by date increasing from bottom to top.

Table 5. Analysis of EPIC X-ray spectra of SXP 1062 as observed on 2013-10-11 in quiescence.

Model	$N_{\rm H}$ (10^{22} cm^{-2})	Γ	$kT_{\rm BB}$ (keV)	$kT_{\rm Thermal}$ (keV)	χ^2/d.o.f.
PL	0.6 ± 0.1	0.67 ± 0.02			1.35 (357)
PL+BB	$0.7^{+0.2}_{-0.3}$	$1.2^{+0.3}_{-0.2}$	$2.1^{+0.1}_{-0.2}$		1.10 (355)
PL+T	$0.7^{+0.3}_{-0.1}$	0.66 ± 0.03		$0.6^{+0.2}_{-0.4}$	1.34 (355)
PL+BB+T	$0.5^{+0.2}_{-0.1}$	$0.8^{+0.2}_{-0.1}$	$1.7^{+0.2}_{-0.2}$	0.8 ± 0.1	1.05 (353)

NOTE: Models with different combinations of components like power law (PL), black body (BB), and thermal plasma emission with SMC abundances (T) were tested. χ^2/d.o.f. lists the reduced χ^2 values, with the number of degrees of freedom in parentheses. Errors are given for a confidence level of 90%. Fig. 3 shows the spectra together with the best-fit model (PL+BB+T).

Table 6. Analysis of ACIS post-outburst X-ray spectra of SXP 1062.

MJD	$N_{\rm H}$ (10^{22} cm^{-2})	Γ	$A_{\rm PL} \times 10^{-5}$ (phot keV^{-1} cm^{-2} s^{-1})	χ^2/d.o.f.
56827.80	177^{+38}_{-31}	$-0.09^{+0.20}_{-0.18}$	$7.5^{+3.2}_{-2.1}$	1.22 (143)
56837.49	42^{+5}_{-5}	$0.4^{+0.1}_{-0.1}$	$19.0^{+3.0}_{-2.5}$	1.10 (241)
56846.30	$31.6^{+3.9}_{-3.5}$	$0.49^{+0.09}_{-0.09}$	$19.3^{+2.9}_{-2.5}$	1.09 (204)
56856.91	$20.2^{+3.6}_{-3.2}$	0.5 ± 0.1	$12.5^{+2.1}_{-1.8}$	0.99 (156)

NOTE: Best-fit parameters for a power-law model. For the definition of χ^2/d.o.f. and errors see Table 5.

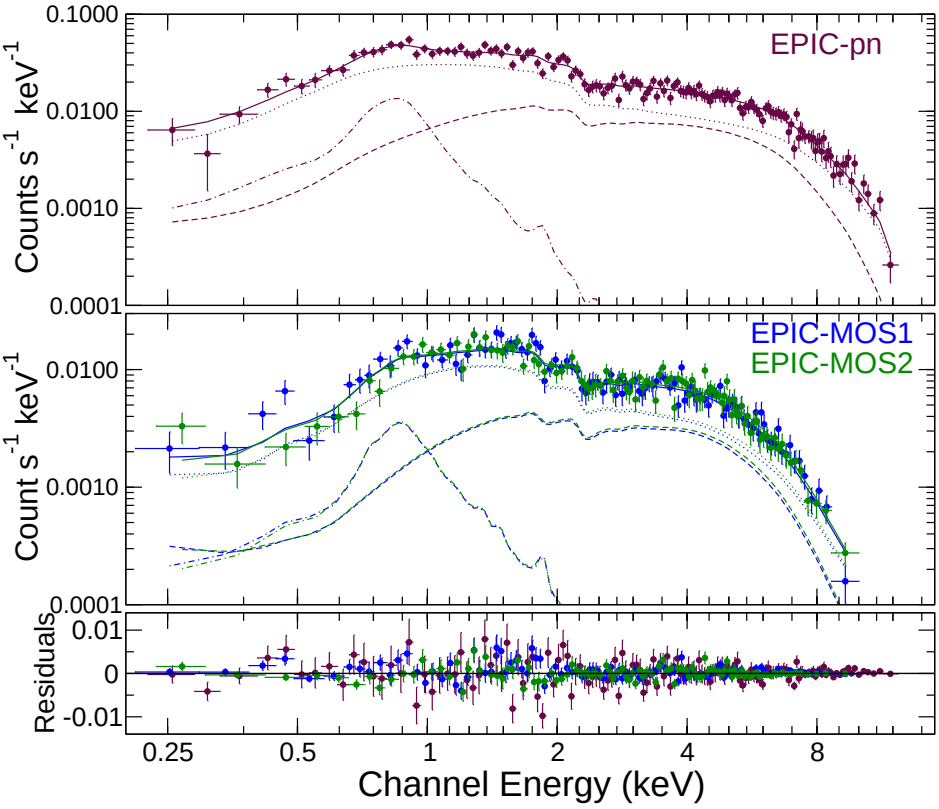

Figure 3. EPIC X-ray spectra of SXP 1062 in quiescence as observed on 2013-10-11 together with the best-fit model (solid lines) of a power law (dotted lines), a black body (dashed lines) and a thermal component (dashed-dotted lines). EPIC-pn/MOS1/MOS2 data are plotted in brown, blue and green. The residuals of the best-fit model with respect to the spectra are plotted in the bottom panel.

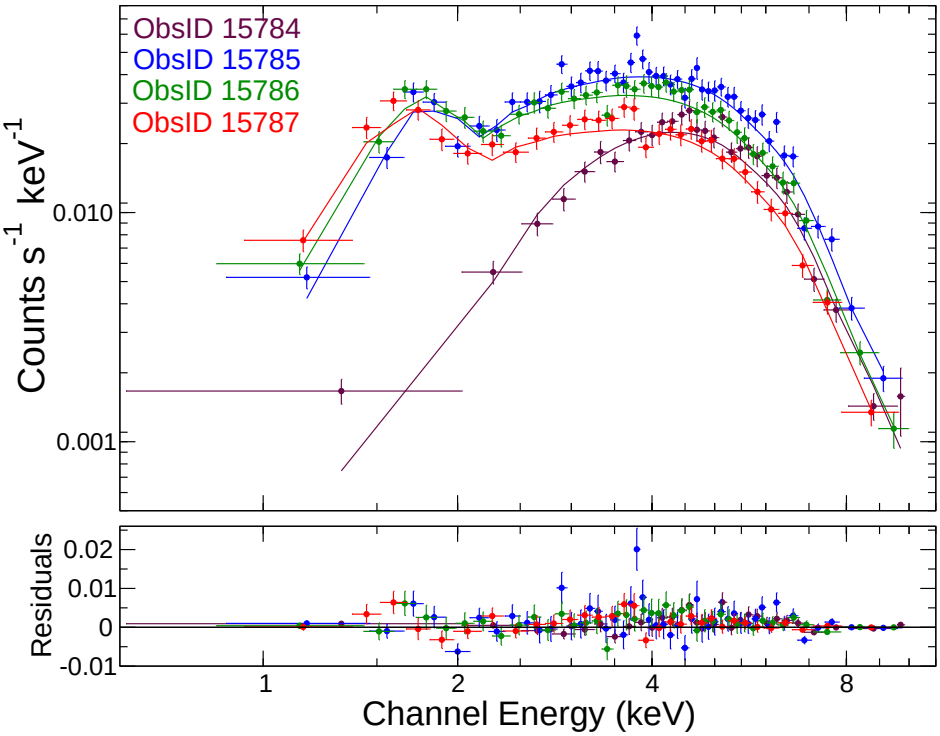

Figure 4. ACIS post-outburst X-ray spectra of SXP 1062 as observed on 2014-06-19 (brown), 2014-06-29 (blue), 2014-07-08 (green), and 2017-07-18 (red). The upper panel shows the spectra (dots with error bars) together with the best-fit model (solid line), while the lower panel shows the residuals of the model with respect to the spectra.

Table 7. Previously published absorbed X-ray fluxes and un-absorbed X-ray luminosities for SXP 1062 together with measurements obtained during this work.

Date	MJD	ΔE	$F_{\rm X}$ (erg cm^{-2} s^{-1})	$L_{\rm X}$ (erg s^{-1})	Reference
2010-03-25	55280	$0.2-12$ keV	$\left(1.7^{+0.2}_{-0.3}\right)\times10^{-12}$	$\left(6.3^{+0.7}_{-0.8}\right)\times10^{35}$	Hénault-Brunet et al. (2012)
2012-10-14	56214	$0.2-10$ keV	$(6.9\pm0.2)\times10^{-12}$	2.6×10^{36}	Sturm et al. (2013)
2013-10-11	56606.80	$0.2-15$ keV	$\left(1.72^{+0.01}_{-0.01}\right)\times10^{-12}$	$(5.7\pm0.1)\times10^{35}$	This work
2014-06-19	56827.80	$0.3-10$ keV	$\left(6.2^{+0.1}_{-0.5}\right)\times10^{-12}$	$(2.6\pm0.1)\times10^{36}$	This work
2014-06-29	56837.49	$0.3-10$ keV	$\left(7.6^{+0.1}_{-0.2}\right)\times10^{-12}$	$(3.0\pm0.1)\times10^{36}$	This work
2014-07-08	56849.30	$0.3-10$ keV	$\left(6.0^{+0.1}_{-0.2}\right)\times10^{-12}$	$(2.4\pm0.1)\times10^{36}$	This work
2014-07-18	56856.91	$0.3-10$ keV	$\left(4.2^{+0.1}_{-0.1}\right)\times10^{-12}$	$(1.6\pm0.1)\times10^{36}$	This work

NOTE: X-ray luminosities are scaled to $DM = 18.7$. The X-ray absorbed flux errors of this work are given for a 68% confidence level, while the un-absorbed X-ray luminosities are given for a 90% confidence level.

Hénault-Brunet et al. (2012) from the analysis of observations obtained in March 2010.

A black-body spectral component characterized by $kT \gtrsim 1.5$ keV seems to be a common feature of X-ray spectra of low luminosity ($L_{\rm X} \lesssim 10^{36}$ erg s^{-1}) and long spin period ($P_{\rm spin} \gtrsim 100$ s) X-ray pulsars (e.g. La Palombara et al. 2013). This component contributes 30-40% of the source flux below 10 keV and implies a small emission radius ($R_{\rm BB} < 0.5$ km) which is typically attributed to the emission from the NS polar caps with a size of $\sim 0.1 R_{\rm NS}$ (Hickox et al. 2004).

The X-ray luminosity of the black-body component in the X-ray spectrum of SXP 1062 in quiescence, $L_{\rm X} \approx (1.8\pm0.1)\times 10^{35}$ erg s^{-1}, amounts to ∼40% of the total X-ray emission below 10 keV, similar to other long-period pulsars. Using the Stefan-Boltzmann law, and the temperature given in Table 5, we estimate the size of the polar cap emission region in SXP 1062 to $R_{\rm BB} = 400^{+140}_{-90}$ m.

The thermal plasma spectral component accounts for ∼20% of the X-ray flux in the softest energy band ($0.2-1.0$ keV). Massive stars with spectral types earlier than B2 are sources of thermal X-ray emission (e.g., Berghoefer et al. 1997). The typical X-ray luminosity of a B0III star does not exceed $\sim 10^{32}$ erg s^{-1} and the bulk of this emission is quite soft with temperatures of about 10^6 K (Raassen et al. 2005; Fossati et al. 2015). Yet, the luminosity of coronal plasma in SXP 1062 is nearly one order of magnitude larger, $L_{\rm X} \approx 6\times10^{33}$ erg s^{-1}. Hence, the intrinsic X-ray emission from the stellar wind of the B0IIIe-type donor star cannot fully account for the thermal radiation observed from this source. We speculate that this soft component originates, at least partly, in the diffuse emission from the maternal SNR.

3.3 Post-outburst X-ray spectra measured by *Chandra*

Chandra obtained four spectra following the outburst detected by *Swift* (see Fig. 1). The first post-outburst observation (ObsID 15784) has significantly lower X-ray flux than the following observation (ObsID 15785). This sharp post-outburst drop in X-ray flux and its subsequent recovery is also evident in the XRT/*Swift* light curve. As discussed later in Section 4.1, the flux decrease is mainly due to the strong increase in the absorbing column.

To model the *Chandra* spectra we started with fitting a simple absorbed power law (see Fig. 4 and Table 6). Subsequently, by analogy with the quiescence spectra we attempted to include a thermal plasma component, but the fits did not improve.

Iron Kα emission is often observed in persistent high-mass X-ray binaries (e.g., Giménez-García et al. 2015) and in transient BeXBs during outbursts (Reig 2011) due to the increase of matter density surrounding the NS. Sturm et al. (2013) found an indication for the presence of an Fe-Kα line in their *XMM-Newton* spectra of SXP 1062 during an outburst in 2012. We also tested for the presence of the iron fluorescence emission line at 6.4 keV in our *Chandra* spectra but this did not lead to a significant improvement of the fit. This non-detection might be due to a poor signal to noise ratio in our ACIS spectra compared to previous *XMM-Newton* observations.

To study changes in the spectral hardness of SXP 1062 we calculated the ratios defined as:

$$HR_{\rm i} = \frac{F_{\rm i+1} - F_{\rm i}}{F_{\rm i+1} + F_{\rm i}}, \qquad (1)$$

where $F_{\rm i}$ is the absorbed flux according to the best-fit spectral model in the corresponding energy band i: $i = 1$ is the softest energy band which corresponds to $0.3-1.0$ keV; $i = 2$ corresponds to $1.0-2.0$ keV; $i = 3$ to $2.0-4.5$ keV; and $i = 4$ to $4.5-10$ keV. The measured fluxes are summarized in Table A2, and the HRs can be found in Table A3.

3.4 X-ray pulse periods and profiles measured by *XMM-Newton* and *Chandra*

To study the pulsational behavior of SXP 1062 we consider the energy bands where the signal from the source dominates over noise, i.e. $0.2-12$ keV for EPIC and $1-8$ keV for ACIS (see Figs. 3 and 4). EPIC-pn and ACIS light curves were extracted with a time binning of 50 s, corrected to the Solar System barycentre using the appropriate software routines, and background subtracted. Over a time interval of ∼29 days

Table 8. Previously published $P_{\rm spin}$ measurements of SXP 1062 together with measurements obtained during this work.

Date	MJD	Instrument	$P_{\rm spin}$ (s)	Reference
2010-03-25	55280	*XMM-Newton*	1062	Hénault-Brunet et al. (2012)
2012-10-14	56214	*XMM-Newton*	1071.01 ± 0.16	Sturm et al. (2013)
2013-10-11	56606.80	EPIC/*XMM-Newton*	1077.97 ± 0.28	This work
2014-06-19	56827.80	ACIS/*Chandra*	1091.1 ± 1.2	This work
2014-06-29	56837.49	ACIS/*Chandra*	1087.1 ± 0.9	This work
2014-07-08	56846.30	ACIS/*Chandra*	1079.3 ± 1.9	This work
2014-07-18	56856.91	ACIS/*Chandra*	1086.0 ± 4.4	This work

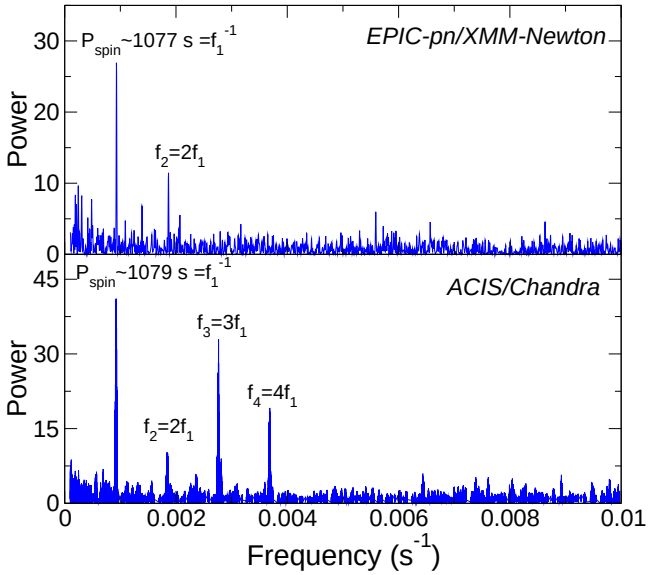

Figure 5. Lomb-Scargle periodograms of EPIC-pn (MJD 56606.80) and merged ACIS (MJDs 56827.80, 56837.49, 56846.30, and 56856.91) observations of SXP 1062 obtained with the PERIOD package within the *Starlink* environment. The main peak of the EPIC-pn periodogram corresponds to $P_{\rm spin} \sim 1077$ s, and the main peak of the merged ACIS light curve corresponds to $P_{\rm spin} \sim 1079$ s. In both cases peaks at harmonic frequencies are seen. A significance calculation with 1000 permutations of the data through a Fisher randomization was performed through the SIG option of PERIOD obtaining a significance level of $\gtrsim 95\%$ for the highest peak in both periodograms.

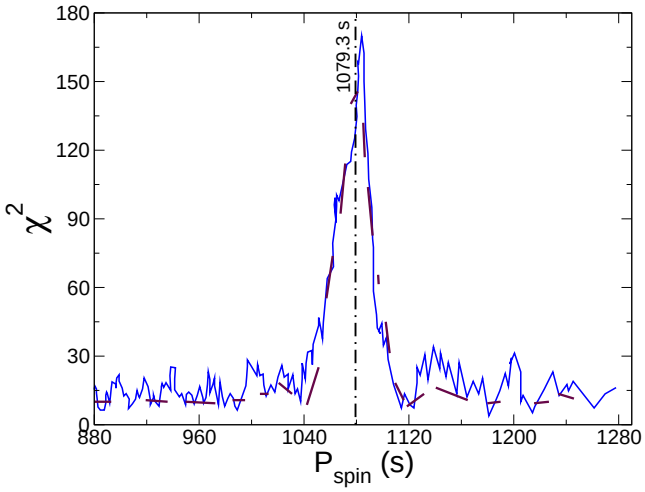

Figure 6. Example of an epoch folding analysis of the ACIS light curve of SXP 1062 from 2014-07-08, performed with the software package DES7. The continuous line is the χ^2 distribution that corresponds to the light curve, the dashed line indicates the χ^2 template function, and the vertical line marks the spin period derived from this observation (for more details see Section 3.2).

and after removing high background intervals, joined ACIS light curves cover 107 ks.

The ACIS and the EPIC-pn light curves were searched for periodic signals between 100 and 10000 s using the SCARGLE routine of the *Starlink* software[5]. This routine performs a fast implementation of the Lomb-Scargle periodogram using Fast Fourier Transforms to increase the speed of computation (Press & Rybicki 1989). We performed a significance calculation by enabling the SIG option of PERIOD which runs a Fisher randomization test with a number of permutations set by the user (1000 in our case) at the same time as the period search is executed. This task gives us result two false alarms probabilities: $FAP1$, which is the probability that, given the frequency search parameters, there is no periodic component present in the data with this period; and $FAP2$, which is the probability that the period is not actually equal to the quoted value but is equal to some other value. We obtained a period of ∼1079 s (see bottom panel of Fig. 5) with $FAP1 = 0$ and $FAP2 = 0$ for the merged ACIS light curve, and a $P_{\rm spin} \sim 1077$ s (see top panel of Fig. 5) with $FAP1 = 0$ and $FAP2 = 0$ for the EPIC-pn light curve. According to the PERIOD user manual, these FAP values imply that the false alarm probabilities lie between 0.00 and 0.01 with 95% confidence. Both periodograms show several peaks (see Fig. 5), the main peak is the spin period of SXP 1062 at that time, while the other peaks correspond to harmonics of the fundamental frequency.

Period determinations for the EPIC-pn and the four ACIS light curves were also performed with an epoch-folding analysis implemented in the DES7 software package (Larsson 1996). This routine folds the data at a number of different test periods (this number was set to 200 periods in this analysis) around an initial input period. The input period is the output obtained with the Lomb-Scargle periodograms shown in Fig. 5. For each period, the χ^2 over the resulting pulse profile is computed, Fig. 6 shows an example of the distribution of χ^2 vs. different test periods for one of our ACIS observations. A best-fit period is determined by fitting a

[5] `http://starlink.jach.hawaii.edu/starlink`

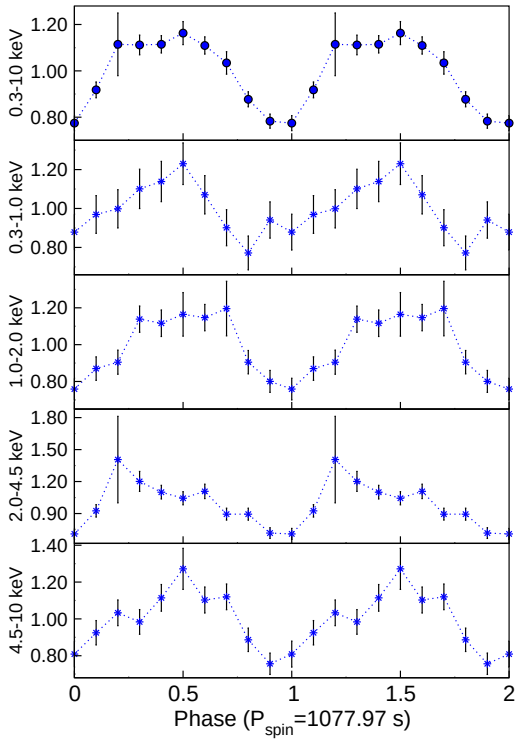

Figure 7. Pulse profiles obtained from EPIC-pn light curves folded over $P_{\rm spin} = 1077.97$ s as observed on 2013-10-11 in quiescence. The top panel shows the pulse profile from the 0.3−10 keV energy band, while in the other panels pulse profiles for different sub-energy bands are presented. Every single light curve is background subtracted and normalised to the average count rate. Phase zero corresponds to the phase of minimum normalized intensity of the folded light curve from the broad energy band. Pulse profiles are plotted twice for clarity.

χ^2 template function to the observed χ^2 distribution (Fig. 6 also shows this χ^2 template). This χ^2 template function is obtained by performing the same analysis to an artificial light curve that takes the time sampling of the data into account and, in an iterative procedure, the pulse shape of the oscillation. Uncertainties are estimated by Monte Carlo simulations. We have performed 500 Monte Carlo simulations in this analysis. A set of synthetic pulse light curves with the same time sampling and noise level as the data are created and analysed. The distribution of the periods determined during these simulations is used as a measurement of period uncertainty. The results of the analysis are shown in Table 8 together with the previous published spin periods for SXP 1062.

To calculate the period derivatives (see Table 9) we assumed a constant spin down/up between every two subsequent $P_{\rm spin}$ measurements of the pulsar. This is a good approximation for *Chandra* given the short time interval between the individual measurements. However, the time interval between the EPIC-pn and the first ACIS measurement is too long with an X-ray outburst occurring in between. Therefore, this derivative can only be considered as an average value during that epoch, or even as a minimum value of the spin down if we consider that the pulsar started to spin up just after the outburst.

X-ray light curves were folded over the corresponding pulse period with the dedicated XRONOS[6] tool *efold*. This routine folds the light curve over a given period and normalizes it to the corresponding average count rate. Pulse profiles obtained from EPIC-pn data are shown in Fig. 7.

X-ray pulsars exhibit a wide variety of pulse shapes which differ from one source to another and which are strongly dependent not only on the energy band but also on the X-ray luminosity. During quiescence the mass accretion rate is steady and low, the gas can freely fall onto the magnetic poles of the NS, and hence form a pencil beam emission. Therefore, X-ray pulsars in quiescence usually show smooth and single-peaked profiles. However, during periastron passage, the accretion of matter results in an increase of the X-ray flux, and consequently pulse profiles usually show the presence of dips at certain pulse phases which are more prominent at soft X-ray energies than at higher energies (e.g., Naik 2013).

Previous quiescence observations of SXP 1062 in 2010 showed indications of a double peak in the pulse profile, while during the outburst observed in 2012 there was only one clear peak at energies above 1 keV (see Fig. 4 of Sturm et al. 2013). This behavior is completely opposite to what is expected. However, during the quiescence observation reported in this paper we observe one smooth peak (see Fig. 7), and there might be a small dip; while, during the *Chandra* post-outburst observations we can clearly see several dips (see Fig. 8); which is what we were expecting.

3.5 Period derivative and orbital Doppler effect

The measured pulse period derivative of any X-ray pulsar is a combination of the intrinsic spin-up or spin-down and the Doppler shift caused by the orbital motion:

$$\dot{P}^{\rm obs}_{\rm spin}(t) = \frac{dP^{\rm obs}_{\rm spin}}{dt} = \frac{dP_{\rm spin}(t)}{dt} + \frac{1}{c}\frac{d}{dt}\left(P_{\rm spin}(t) v_{\rm orb}(t)\right), \quad (2)$$

where $v_{\rm orb}$ is the radial velocity, i.e. the projected orbital velocity along the line of sight:

$$v_{\rm orb}(t) = \frac{2\pi a_{\rm X} \sin i}{P_{\rm orb}\sqrt{1-e^2}}\left(\cos(\theta(t)+\omega) + e\cos(\omega)\right), \quad (3)$$

where $a_{\rm X} \sin i$ is the projected semi-major axis of the pulsar, $P_{\rm orb}$ is the orbital period, e is the eccentricity, and ω is the longitude of periastron. The true anomaly $\theta(t)$ is found by solving Kepler's equation.

We check whether the spin period derivative obtained in this work, and also during previous analyses, could be explained as a consequence of the orbital motion of the pulsar along its binary orbit. Following Eq. 2 we calculate the period derivative caused by the orbital Doppler effect assuming no intrinsic changes in the actual spin period and all the change we observe is only due to the orbital motion. This derivative depends on the orbital parameters of the binary system.

Unfortunately, the orbit of SXP 1062 is not known. Therefore, we estimate an appropriate range of possible orbital parameters as follows:

(i) $P_{\rm spin} = 1062$ s as published by Hénault-Brunet et al. (2012) for simplicity.

[6] `http://heasarc.gsfc.nasa.gov/docs/xanadu/xronos/xronos.html`

Table 9. Previously published $\dot{P}_{\rm spin}$ measurements of SXP 1062 together with measurements obtained during this work.

MJD	Δt (days)	$\dot{P}_{\rm spin}$ (s/d)	Reference	Confidence
55280	18	0.24 ± 0.07	Haberl et al. (2012)	99.999%
56214	915	0.0062 ± 0.0012	Sturm et al. (2013)	43.658%
56410.4	393	0.0177 ± 0.0009	This work	76.465%
56717.4	221	0.059 ± 0.006	This work	95.982%
56832.5	9	-0.45 ± 0.16	This work	99.999%
56841.5	9	-0.86 ± 0.23	This work	99.999%
56851.5	11	0.61 ± 0.44	This work	99.999%

NOTE: MJDs of the $\dot{P}$ values obtained during this work are the mid-time value between two spin period measurements. The second column (Δt) indicates the time interval for which the spin period derivative was calculated. The last column is the probability of the spin derivative to be intrinsic according to the probability distribution shown in Fig. 9.

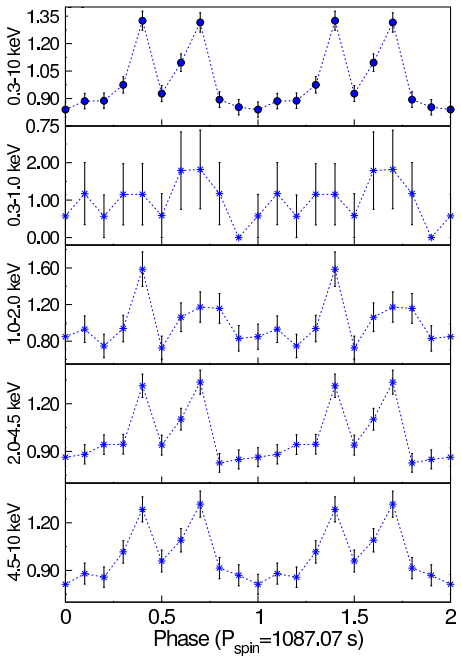

Figure 8. SXP 1062 pulse profile of ACIS post-outburst light curve folded over the corresponding spin period (shown in the x axis of the corresponding figure) as observed on 2014-06-29. The upper panel shows the pulse profile over the whole energy band, while the rest of the panels show pulse profiles for different sub-energy bands. Every single light curve is background subtracted and normalized to the corresponding average count rate. Phase zero corresponds to the phase of minimum normalized intensity of the folded light curve that corresponds to the whole energy band. Pulse profiles are reported twice for clarity.

(ii) $P_{\rm orb} = 668 \pm 10$ d (see Section 3.1).
(iii) $0.4 \lesssim e \lesssim 0.88$

To estimate a lower limit for the eccentricity we assume that the progenitor binary had a circular orbit and zero kick velocity. Then, after the SN explosion:

$$e = \frac{\Delta M}{M_1 + M_2 - \Delta M} \quad (4)$$

(Verbunt & Phinney 1995), where M_1 and M_2 are the masses of the stars before the SN explosion and ΔM is the mass loss of the system during this explosion. Hénault-Brunet et al. (2012) estimated an evolutionary mass of $M_1 \sim 15\,{\rm M}_\odot$ for the Be-companion of SXP 1062. Assuming that the NS in SXP 1062 has the canonical mass of a NS (we neglect the difference between baryonic and gravitational masses), i.e., $1.4\,{\rm M}_\odot = M_2 - \Delta M$ (e.g., Lattimer & Steiner 2014), we estimate the mass loss to be $\Delta M > 14\,{\rm M}_\odot$.

Consequently, the eccentricity is expected to be close to unity. For our purpose we adopt a conservative approach and use as lower limit for the eccentricity $e > 0.4$. Note, that lower eccentricity values for the orbit result in a higher probability for the spin period derivative to be intrinsic. We adopt $e < 0.88$, which is the highest eccentricity known to date for a BeXB (2S 1845−0242; Finger et al. 1999), as the upper limit for the eccentricity. Consequently, we assume the eccentricity to be uniformly distributed between 0.4 and 0.88.

(iv) The longitude of periastron (ω) is a geometric effect. Thus, we allow any value between -180° and +180° and assume a uniform distribution.

(v) Following the third Kepler law, the semi-major axis of the orbit of the NS is $a_{\rm X} = 1713.46$ light-s. The orbital inclination is not known, therefore, we let it vary between 0 and 90°.

We performed 100000 Monte Carlo simulations where we calculated the spin period derivative choosing randomly the orbital parameters within the previously estimated ranges. The maximum of the simulated $\dot{P}_{\rm spin}(t)$ for each Monte Carlo run is binned into a histogram that results in a distribution of probability to observe a certain $\dot{P}_{\rm spin}$-value caused by the orbital motion of the binary. Fig. 9 shows this distribution of probabilities. We assume pulse period derivatives out of this distribution to be intrinsic to the pulsar, while those which are within this distribution have different probabilities of being intrinsic depending on their position with respect to the distribution (see last column of Table 9).

4 DISCUSSION

4.1 The Be star decretion disc and the X-ray flux

The Hα line is the primary indicator for the presence of a decretion disc around a Be star and its EW provides information about the size of this disc. In Section 2.2.1 we presented *SALT* observations at different epochs which allow us to study the time evolution of Hα and Hβ emission lines and their EW. The non-split shape of Balmer lines and

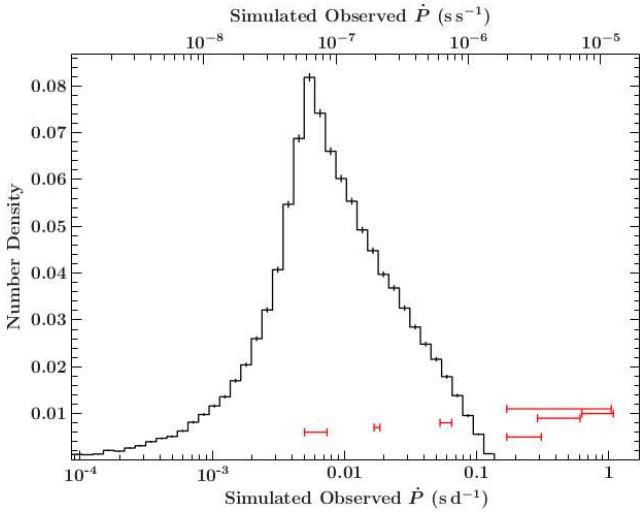

Figure 9. Distribution of expected $\dot{P}$-values caused by orbital Doppler shifts according to the range of values for the orbital parameters estimated for SXP 1062 (see Section 3.5). The red horizontal lines indicate the position of the spin period derivatives given in Table 9.

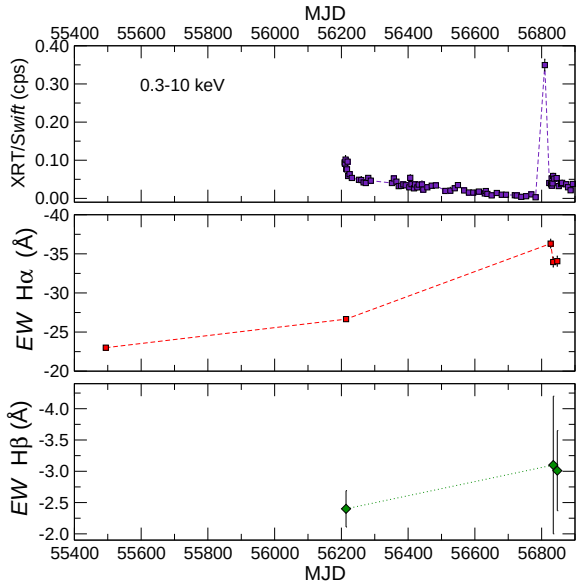

Figure 10. SXP 1062 XRT/*Swift* flux in the energy range 0.3 – 10 keV in the top panel. Medium and bottom panels show the evolution of the *EW* of Hα and Hβ of SXP 1062 respectively (Table 3).

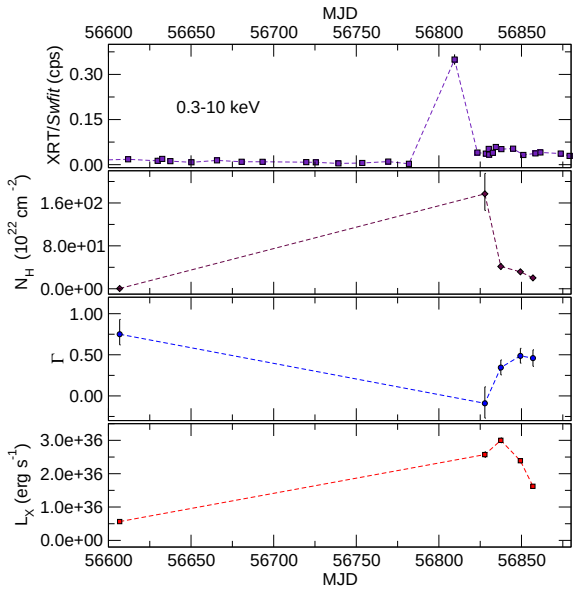

Figure 11. *Top panel:* SXP 1062 XRT/*Swift* flux in the energy range 0.3 – 10 keV. *Second panel:* SXP 1062 absorption column ($N_{\rm H}$) of EPIC and ACIS observations (values from Tables 5 and 6). *Third panel:* SXP 1062 photon index (Γ) of EPIC and ACIS spectra (values from Tables 5 and 6). *Bottom panel:* SXP 1062 X-ray 0.3 – 10 keV luminosities obtained from EPIC and ACIS spectra (values from Table 7).

the time evolution of absorbing column deduced from X-ray spectra indicates that we likely observe the Be disc face on. Reig et al. (1997) and, most recently Haberl & Sturm (2016) showed a correlation between the orbital periods and the *EW* of the Hα line in BeXBs which follows a linear trend with larger Hα emission for longer orbital periods. This correlation was explained in the framework of the truncation disc model. The disc truncation is responsible for the so-called Type II X-ray outbursts, and inhibits the growth of the decretion disc (Negueruela et al. 2001; Okazaki & Negueruela 2001). Interestingly, SXP 1062 does not follow the Hα-orbital period correlation, likely its Be-disc is smaller than usual for its orbital period.

Fig. 10 shows that the *EW* of Hα and Hβ in SXP 1062 keeps increasing over years, however it drops after the X-ray outburst, as can indeed be expected for a BeXB. This change provides further confirmation that the NS interacts with the Be-disc during the outburst. However, the decrease in the disc size after the outburst is not dramatic, indicating that the disc of the donor star in SXP 1062 is likely not truncated during the outburst.

4.2 Evolution of the spectral parameters

As shown in sections 3.2 and 3.3, the basic X-ray spectrum of SXP 1062 is an absorbed power law. This is similar to X-ray spectra of other BeXBs in the SMC (Haberl et al. 2008).

Our data set allows us to investigate how the X-ray spectrum of SXP 1062 changes in the different luminosity regimes, i.e. during quiescence and post-outburst. The time evolution of absorbing column and power-law index are shown in Figure 11. In this figure one can see a strong increase in the absorption column immediately after the outburst, followed by a sharp decrease. At the same time, the spectrum initially softens (power-law index drops), and then hardens post-outburst.

In combination, the time evolution of absorbing column and power-law index points to the accumulation of matter in the vicinity of the X-ray source towards and during the outburst, and a fast depletion afterwards.

We tentatively interpret this behavior in the framework of a model that assumes that the outburst is triggered by the passage of the NS through the Be-disc. The orbit of the NS

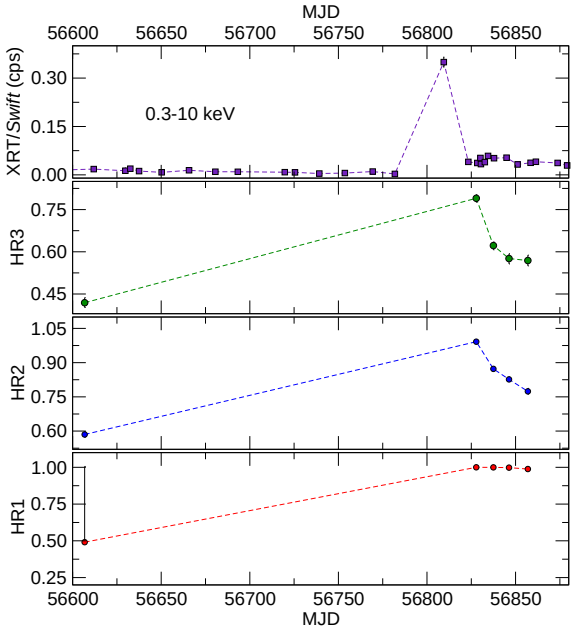

Figure 12. SXP 1062 XRT/*Swift* flux in the energy range 0.3 − 10 keV in the top panel. Second, third and bottom panels show hardness ratios calculated following Eq. 1 which are given in Table A3.

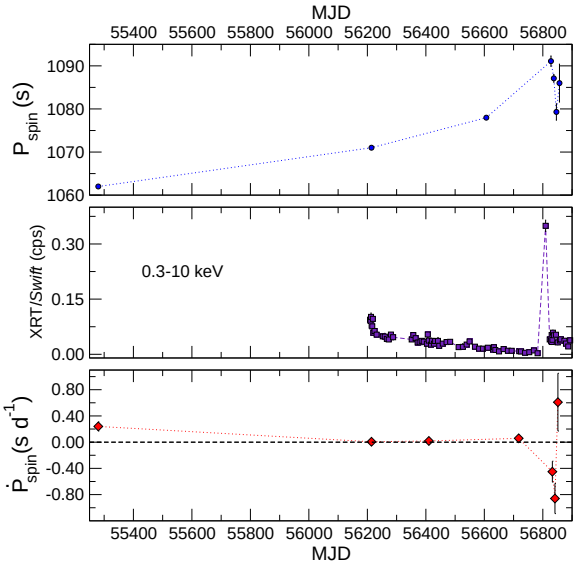

Figure 13. *Top panel:* Temporal evolution of the pulse period of SXP 1062 (Table 8). *Middle panel:* XRT/*Swift* 0.3 − 10 keV X-ray light curve of SXP 1062. *Bottom panel:* SXP 1062 spin period derivative as a function of time (Table 9).

is probably inclined to the disc. According to this scenario, after the NS pierces the Be-disc, it is observed through the disc material. As the time progresses, the column density decreases to its low quiescence value. Similar behavior is also observed in other systems, e.g. SXP 5.05 (Coe et al. 2015). Future work, especially hydrodynamic modelling of winds from fast rotating Be stars, shall clarify whether the scenario we consider here is viable.

4.3 Spin period evolution and magnetic field

In this work we present new spin-period measurements for SXP 1062. With these new data we confirm that the pulsar appears to be spinning down continuously since it was discovered in March 2010 until at least, October 2013, which is the date of our quiescence *XMM-Newton* observation. Our first *Chandra* post-outburst spin period (1091 s; 2014-06-19) is longer than observed in October 2013 (1077.97 s), consequently, the pulsar could even have been spinning down until some time before the outburst detected by *Swift* in June 2014 (see Fig. 13). However, we have observed for the first time a spin up for SXP 1062 just after the outburst detected by *Swift*. We also observe how SXP 1062 seems to recover its usual spin down in the last observation. To confirm this spin down we would need more observations.
Next we estimate the magnetic field of SXP 1062 according to the observed spin period evolution and the relatively new model of quasi-spherical accretion developed by Shakura et al. (2012).

4.3.1 Spin period equilibrium hypothesis

We start with a magnetic field estimate based on the hypothesis of spin equilibrium. It is supposed that in a stationary situation spin-up and spin-down torques balance each other, and so the spin period is equal to the equilibrium value (Davidson & Ostriker 1973). This quantity depends on several parameters of the system (accretion rate, properties of the accretion flow, parameters of the binary system, etc.). In particular, it depends on the magnetic field of the NS. Therefore, if all other parameters are more or less well known we can estimate the magnetic field using the following equation from Postnov et al. (2015) (see details on the derivation of this formula in Shakura et al. 2013):

$$P_{\rm eq} = 940\,\mu_{30}^{12/11}(P_{\rm orb}/10\,{\rm d})\dot{M}_{16}^{-4/11}v_{\rm w8}^{4}\,{\rm s}. \qquad (5)$$

Here $v_{\rm w8}$ is the stellar wind velocity in units of 10^8 cm s^{-1}, $\dot{M}_{16}$ is the mass accretion rate in units of $10^{16}\,{\rm g\,s^{-1}}$, and μ_{30} is the magnetic moment in units of $10^{30}\,{\rm G\,cm^3}$ ($\mu_{30}=1$ corresponds to $B=10^{12}$ G on the equator for the standard $R_{\rm NS}\sim 10$ km; note, that for $R_{\rm NS}\sim 15$ km (Bogdanov 2013), the field B would be half an order of magnitude smaller for the same μ). This equation is applicable to systems with quasi-spherical accretion with $\dot{M}\lesssim 10^{16}\,{\rm g\,s^{-1}}$ (so-called *settling accretion regime* which is applicable to X-ray pulsars with $L_{\rm X}\lesssim 10^{36}\,{\rm erg\,s^{-1}}$, see Shakura et al. 2012).
Substituting the parameters for SXP 1062 we obtain:

$$\mu_{30}\approx 7\left(\frac{\dot{M}}{5\times10^{15}\,{\rm g\,s^{-1}}}\right)^{1/3}\left(\frac{v_{\rm w}}{200\,{\rm km\,s^{-1}}}\right)^{-11/3}. \qquad (6)$$

Assuming wind velocities $v_{\rm w}\sim 200\,{\rm km\,s^{-1}}$, which is typical for quasi-spherical winds observed from Be stars (Waters et al. 1988), the estimated magnetic field has a standard value of $B\sim 7\times10^{12}$ G. If we assume higher wind velocities the magnetic field would even be lower. Consequently, according to this estimate, we are not dealing with a present-day magnetar.

4.3.2 Out of equilibrium hypothesis

(i) Long-term spin down

We have seen that the pulsar might be out of equilibrium because we observe a continuous spin down over years (see Fig. 13). Therefore, we can use the data which correspond to the spin down of the pulsar to obtain another estimate of the magnetic field. Again, we use an equation from Postnov et al. (2015):

$$\dot{P}_{\rm sd} \approx 7\times10^{-3}\left(\frac{\Pi_{\rm sd}}{7}\right)\left(\frac{\dot{M}}{5\times10^{15}\,{\rm g}\,s^{-1}}\right)^{3/11}\left(\frac{P_{\rm spin}}{1080\ {\rm s}}\right)\mu_{30}^{13/11}\,{\rm s\,d^{-1}} \quad (7)$$

Here $\Pi_{\rm sd}$ is a parameter of the theory of settling accretion, its typical value is ∼5−10. Postnov et al. (2015, and references therein) demonstrate that this parameter does not change much from system to system. As we cannot derive it independently, we choose a typical value $\Pi_{\rm sd} = 7$. The variation of this parameter might have a very limited (less than a factor of two) influence on the estimate of μ. From the observations of SXP 1062 we can estimate an average $\dot{P}_{\rm sd} \approx 0.02$ s d^{-1}. Then we obtain $\mu_{30} \approx 3$, which corresponds to $B \sim 3\times10^{12}$ G. Taking into account many uncertainties in models and parameters, this result is in reasonable correspondence with the estimate obtained above from the equilibrium period. Note, that these values are in correspondence with the saturation value for magnetar field decay (Pons et al. 2009; Gourgouliatos & Cumming 2014).

(ii) Spin up during the outburst

Finally, we calculate the magnetic field using the spin up $\dot{P}_{\rm su}$ observed during the outburst detected by our *Swift* monitoring campaign. For this case we can neglect the braking torque. Then the equation for the evolution of the period reads:

$$\dot{P}_{\rm su} = P_{\rm spin}^2 P_{\rm orb}^{-1}\dot{M}R_{\rm B}^2 I^{-1}, \quad (8)$$

where I is the moment of inertia of the NS, we assume a standard value 10^{45} g cm^2 for it. $R_{\rm B}$ is the Bondi radius. This equation provides an upper limit for the modulus of $\dot{P}_{\rm su}$, but realistic values are not much smaller (Lipunov 1992).

Note, that the maximum spin up happens during outbursts which appear close to the periastron. Then, we cannot take an average value for $R_{\rm B}$ which depends on $v_{\rm orb}$ and hence on the eccentricity. For larger eccentricities we obtain larger spin up. If we take $e = 0.7$, $\dot{M} = 10^{17}$ g s^{-1}, stellar mass $15\,M_\odot$ and $v_{\rm w} = 200$ km s^{-1}, we obtain $\dot{P}_{\rm su} \approx 0.5$ s d^{-1}. The observed average value for SXP 1062 is $\dot{P}_{\rm su} \sim 0.5$ s d^{-1}. Then, we can conclude that the spin-up can be described by relatively highly eccentric orbits, which coincides with the estimation we have performed of the orbital parameters (see Section 3.5).

These simple estimations agree within uncertainties with those presented in Sec. 3 and are in line with the theoretical expectations. Therefore, we can explain the spin period derivative observed in SXP 1062 applying the theory of quasi-spherical accretion (Shakura et al. 2012) without the need of an extremely strong magnetic field, such as the one observed in an accreting magnetar. Future and in depth theoretical modelling of SXP 1062 is necessary to fully verify this conjecture.

4.4 On the classification of SXP 1062

BeXBs are classified into two broad subgroups: transient BeXBs and persistent BeXBs (Reig 2011), which may overlap in part of their properties. In Table 10 we summarize the key characteristics of these sub-groups.

SXP 1062 has properties that are shared by both of these sub-groups. Its large X-ray luminosity in quiescence (see Table 7), the long binary orbital period $P_{\rm orb} = 668 \pm 10$ days, and its long pulse period $P_{\rm spin} \sim 1070$ s, are typical for persistent BeXBs. Also, to date no known BeXB system containing a NS with $P_{\rm spin} > 100$ s has an eccentricity above 0.5 (Townsend et al. 2011). On the other hand, the Type I outburst reported in this work, although moderate, is a characteristic of transient BeXBs. Therefore, the properties of SXP 1062 suggest that systems exist which can be classified as member of both groups and that transient and persistent BeXBs are not completely separated sub-groups.

5 SUMMARY AND CONCLUSIONS

In this work we present a coordinated optical and X-ray study of the X-ray pulsar SXP 1062 during quiescence and outburst. The main results of our study are:

– We observed a third Type I outburst in SXP 1062. The outburst occurred at a regular interval from two previously observed. The binary period is constrained to $P_{\rm orb} \approx 668 \pm 10$ d. Type I outbursts are characteristic for transient BeXB. Thus SXP 1062 shares observational characteristics with persistent as well as transient BeXBs.

– The profiles of the Hα line indicate that we likely observe the Be-disc face on, while the temporal evolution of its *EW* shows that the disc is not truncated in the aftermath of the outburst.

– We confirm the earlier reports on the presence of a black body spectral component in the quiescent X-ray spectrum of SXP 1062.

– Our analysis of the pre- and post-outburst spectra reveals an abrupt increase in the absorption column just after the outburst. Taking into account the Hα line profile, we propose that the disc of the Be star is observed face on, while the orbit of the NS is inclined to the disc.

– Studies of the NS spin evolution reveal that the NS had been intrinsically spinning down at least from March 2010 until October 2013. We report a brief post-outburst spin up of the X-ray pulsar.

– We estimate the magnetic field for SXP 1062, assuming different hypotheses for the spin period evolution (e.g., close to equilibrium, out of equilibrium) and the quasi-spherical accretion model (Shakura et al. 2012). From these calculations we find no need for an extremely high magnetic field at present day for the pulsar in SXP 1062.

ACKNOWLEDGMENTS

SBP thanks Profs. N.I. Shakura and K.A. Postnov for discussions. AGG and LO are supported by the Deutsches Zen-

Table 10. Main properties of the two established Be X-ray binaries sub-groups.

	Transient	**Persistent**
Quiescence $L_{\rm X}$	$\lesssim 10^{33}\,{\rm erg\,s^{-1}}$	$\sim 10^{34-35}\,{\rm erg\,s^{-1}}$
Outbursts	Two different types Type I: Periodic with orbital period and $L_{\rm X} \lesssim 10^{37}\,{\rm erg\,s^{-1}}$ Type II: Random with $L_{\rm X} \sim 10^{38}\,{\rm erg\,s^{-1}}$	Relatively quiet systems Sporadic and non-predictable increases of $L_{\rm X}$ Increases of less than one order of magnitude
Pulse period $P_{\rm spin}$	$\sim 10\,{\rm s}$	$\gtrsim 200\,{\rm s}$
Orbital period $P_{\rm orb}$	$20 \lesssim P_{\rm orb} \lesssim 100\,{\rm d}$	$\gtrsim 200\,{\rm d}$
Eccentricity e	$\gtrsim 0.3$	$\lesssim 0.2$

NOTE: The data presented in this table have been collected from the following papers: Campana et al. (2002); Okazaki & Negueruela (2001); Negueruela et al. (2001); Reig (2011); Knigge et al. (2011); Cheng et al. (2014)

trum für Luft und Raumfahrt (DLR) under contracts No. FKZ 50 OR 1404, and No. FKZ 50 OR 1302 and grants. MK acknowledges funding by the Bundesministerium für Wirtschaft und Technologie under Deutsches Zentrum für Luft- und Raumfahrt grants 50 OR 1113 and 50 OR 1207. SBP is supported by the Russian Science Foundation grant 14-12-00146 MPES received funding through the Claude Leon Foundation Postdoctoral Fellowship program and the National Research Foundation. The scientific results reported in this article are based on observations made by the *Chandra*, *XMM-Newton*, and *Swift* X-ray observatories, the Southern African Large Telescope (*SALT*), and the OGLE III photometry data base.

REFERENCES

Arnaud K. A., 1996, in Jacoby G. H., Barnes J., eds, Astronomical Data Analysis Software and Systems V Vol. 101 of Astronomical Society of the Pacific Conference Series, XSPEC: The First Ten Years. p. 17
Berghoefer T. W., Schmitt J. H. M. M., Danner R., Cassinelli J. P., 1997, A&A, 322, 167
Bird A. J., Coe M. J., McBride V. A., Udalski A., 2012, MNRAS, 423, 3663
Bogdanov S., 2013, ApJ, 762, 96
Campana S., Stella L., Israel G. L., Moretti A., Parmar A. N., Orlandini M., 2002, ApJ, 580, 389
Cheng Z.-Q., Shao Y., Li X.-D., 2014, ApJ, 786, 128
Cignoni M., Sabbi E., Nota A., Tosi M., Degl'Innocenti S., Moroni P. G. P., Angeretti L., Carlson L. R., Gallagher J., Meixner M., Sirianni M., Smith L. J., 2009, AJ, 137, 3668
Coe M. J., Bartlett E. S., Bird A. J., Haberl F., Kennea J. A., McBride V. A., Townsend L. J., Udalski A., 2015, MNRAS, 447, 2387
Davidson K., Ostriker J. P., 1973, ApJ, 179, 585
Evans C. J., Howarth I. D., Irwin M. J., Burnley A. W., Harries T. J., 2004, MNRAS, 353, 601
Finger M. H., Bildsten L., Chakrabarty D., Prince T. A., Scott D. M., Wilson C. A., Wilson R. B., Zhang S. N., 1999, ApJ, 517, 449
Fossati L., Castro N., Morel T., Langer N., Briquet M., Carroll T. A., Hubrig S., Nieva M. F., Oskinova L. M., 2015, A&A, 574
Fu L., Li X.-D., 2012, ApJ, 757, 171
Garmire G., 2001, in Giacconi R., Serio S., Stella L., eds, X-ray Astronomy 2000 Vol. 234 of Astronomical Society of the Pacific Conference Series, Results from the Chandra X-ray Observatory using the ACIS instrument. p. 15
Gehrels et al. 2004, ApJ, 611, 1005
Giménez-García A., Torrejón J. M., Eikmann W., Martínez-Núñez S., Oskinova L. M., Rodes-Roca J. J., Bernabéu G., 2015, A&A, 576, A108
Gourgouliatos K. N., Cumming A., 2014, MNRAS, 438, 1618
Haberl F., Eger P., Pietsch W., 2008, A&A, 489, 327
Haberl F., Sturm R., 2016, A&A, 586, A81
Haberl F., Sturm R., Filipović M. D., Pietsch W., Crawford E. J., 2012, A&A, 537, L1
Hénault-Brunet V., Oskinova L. M., Guerrero M. A., Sun W., Chu Y.-H., Evans C. J., Gallagher III J. S., Gruendl R. A., Reyes-Iturbide J., 2012, MNRAS, 420, L13
Hickox R. C., Narayan R., Kallman T. R., 2004, ApJ, 614, 881
Ikhsanov N. R., 2012, MNRAS, 424, L39
Jones C. E., Sigut T. A. A., Porter J. M., 2008, MNRAS, 386, 1922
Knigge C., Coe M. J., Podsiadlowski P., 2011, Nature, 479, 372
Kobulnicky H. A., Nordsieck K. H., Burgh E. B., Smith M. P., Percival J. W., Williams T. B., O'Donoghue D., 2003, in Iye M., Moorwood A. F. M., eds, Instrument Design and Performance for Optical/Infrared Ground-based Telescopes Vol. 4841 of Society of Photo-Optical Instrumentation Engineers (SPIE) Conference Series, Prime focus imaging spectrograph for the Southern African large telescope: operational modes. pp 1634–1644
La Palombara N., Mereghetti S., Sidoli L., Tiengo A., Esposito P., 2013, Central European Astrophysical Bulletin, 37, 277
Larsson S., 1996, A&AS, 117, 197
Lattimer J. M., Steiner A. W., 2014, ApJ, 784, 123
Lipunov V. M., 1992, Astrophysics of Neutron Stars
Nagase F., 1989, PASJ, 41, 1
Naik S., 2013, in Das S., Nandi A., Chattopadhyay I., eds,

Astronomical Society of India Conference Series Vol. 8 of Astronomical Society of India Conference Series, X-ray and infrared properties of Be/X-ray binary pulsars. pp 103–108
Negueruela I., Okazaki A. T., Fabregat J., Coe M. J., Munari U., Tomov T., 2001, A&A, 369, 117
Okazaki A. T., Negueruela I., 2001, A&A, 377, 161
Oskinova L. M., Sun W., Evans C. J., Hénault-Brunet V., Chu Y.-H., Gallagher III J. S., Guerrero M. A., Gruendl R. A., Güdel M., Silich S., Chen Y., Nazé Y., Hainich R., Reyes-Iturbide J., 2013, ApJ, 765, 73
Pons J. A., Miralles J. A., Geppert U., 2009, A&A, 496, 207
Popov S. B., Turolla R., 2012, MNRAS, 421, L127
Porter J. M., Rivinius T., 2003, PASP, 115, 1153
Postnov K. A., Mironov A. I., Lutovinov A. A., Shakura N. I., Kochetkova A. Y., Tsygankov S. S., 2015, MNRAS, 446, 1013
Press W. H., Rybicki G. B., 1989, ApJ, 338, 277
Raassen A. J. J., Cassinelli J. P., Miller N. A., Mewe R., Tepedelenlioğlu E., 2005, A&A, 437, 599
Reig P., 2011, APSS, 332, 1
Reig P., Fabregat J., 2015, A&A, 574, A33
Reig P., Fabregat J., Coe M. J., 1997, A&A, 322, 193
Russell S. C., Dopita M. A., 1992, ApJ, 384, 508
Schmidtke P. C., Cowley A. P., Udalski A., 2012, The Astronomer's Telegram, 4596, 1
Shakura N., Postnov K., Kochetkova A., Hjalmarsdotter L., 2012, MNRAS, 420, 216
Shakura N. I., Postnov K. A., Kochetkova A. Y., Hjalmarsdotter L., 2013, Physics Uspekhi, 56, 321
Smith R. K., Brickhouse N. S., Liedahl D. A., Raymond J. C., 2001, ApJ, 556, L91
Strüder et al. 2001, A&A, 365, L18
Sturm R., Haberl F., Oskinova L. M., Schurch M. P. E., Hénault-Brunet V., Gallagher J. S., Udalski A., 2013, A&A, 556, A139
Townsend L. J., Coe M. J., Corbet R. H. D., Hill A. B., 2011, MNRAS, 416, 1556
Turner et al. 2001, A&A, 365, L27
Udalski A., 2008, Acta Astronomica, 58, 187
Verbunt F., Phinney E. S., 1995, A&A, 296, 709
Waters L. B. F. M., van den Heuvel E. P. J., Taylor A. R., Habets G. M. H. J., Persi P., 1988, A&A, 198, 200
Wilms J., Allen A., McCray R., 2000, ApJ, 542, 914

APPENDIX A: ADDITIONAL TABLES

Table A1. SXP 1062 un-absorbed X-ray luminosities in the standard sub-energy bands as observed with EPIC and ACIS according to the best-fit spectral models (see Tables 5 and 6).

MJD		$L(0.3-1.0\,\mathrm{keV})$ $(10^{34}\,\mathrm{erg\,s^{-1}})$	$L(1.0-2.0\,\mathrm{keV})$ $(10^{34}\,\mathrm{erg\,s^{-1}})$	$L(2.0-4.5\,\mathrm{keV})$ $(10^{35}\,\mathrm{erg\,s^{-1}})$	$L(4.5-10\,\mathrm{keV})$ $(10^{36}\,\mathrm{erg\,s^{-1}})$	$L(10-15\,\mathrm{keV})$ $(10^{35}\,\mathrm{erg\,s^{-1}})$
56606.80	EPIC/*XMM-Newton*	$1.71^{+0.13}_{-0.12}$	3.01 ± 0.07	$1.10^{+0.022}_{-0.021}$	0.271 ± 0.009	2.030 ± 0.040
56827.80	ACIS/*Chandra*	1.92 ± 0.06	6.80 ± 0.22	3.96 ± 0.13	2.09 ± 0.07	5.69 ± 0.19
56837.49	ACIS/*Chandra*	5.75 ± 0.14	14.31 ± 0.34	5.93 ± 0.14	2.21 ± 0.05	5.14 ± 0.12
56846.30	ACIS/*Chandra*	6.17 ± 0.16	13.66 ± 0.36	5.07 ± 0.13	1.684 ± 0.044	3.73 ± 0.10
56856.91	ACIS/*Chandra*	3.97 ± 0.12	8.98 ± 0.28	$3.40^{+0.10}_{-0.11}$	1.153 ± 0.036	3.04 ± 0.10

NOTE: We assume a distance modulus of 18.7 for the luminosity, which is the appropriate distance for the Wing of the SMC (e.g., Cignoni et al. 2009). The un-absorbed X-ray luminosities are given with a 90% confidence level. ACIS X-ray luminosities in the energy range $10-15\,\mathrm{keV}$ are extrapolated values from the spectral model for comparison with the EPIC X-ray luminosity value in this energy range.

Table A2. SXP 1062 absorbed X-ray fluxes in the standard sub-energy bands as observed with EPIC and ACIS according to the best-fit spectral models (see Tables 5 and 6).

MJD		$F(0.3-1.0\,\mathrm{keV})$ $(10^{-14}\,\mathrm{erg\,cm^{-2}\,s^{-1}})$	$F(1.0-2.0\,\mathrm{keV})$ $(10^{-14}\,\mathrm{erg\,cm^{-2}\,s^{-1}})$	$F(2.0-4.5\,\mathrm{keV})$ $(10^{-13}\,\mathrm{erg\,cm^{-2}\,s^{-1}})$	$F(4.5-10\,\mathrm{keV})$ $(10^{-13}\,\mathrm{erg\,cm^{-2}\,s^{-1}})$	$F(10-15\,\mathrm{keV})$ $(10^{-13}\,\mathrm{erg\,cm^{-2}\,s^{-1}})$
56606.80	EPIC/*XMM-Newton*	$2.747^{+0.025}_{-0.101}$	$8.04^{+0.09}_{-0.11}$	$3.07^{+0.08}_{-0.07}$	$7.50^{+0.15}_{-0.13}$	$5.653^{+0.020}_{-0.017}$
56827.80	ACIS/*Chandra*	$\left(3.10^{+0.27}_{-0.30}\right) \times 10^{-13}$	$0.27^{+0.06}_{-0.07}$	$6.532^{+0.065}_{-0.028}$	$55.5^{+1.5}_{-3.4}$	$15.6^{+0.8}_{-1.3}$
56837.49	ACIS/*Chandra*	$\left(2.3^{+1.2}_{-0.6}\right) \times 10^{-3}$	$9.60^{+0.30}_{-0.41}$	$14.11^{+0.22}_{-0.24}$	$60.5^{+1.5}_{-0.2}$	$14.2^{+0.7}_{-0.6}$
56846.30	ACIS/*Chandra*	$\left(1.28^{+0.45}_{-0.38}\right) \times 10^{-2}$	$11.83^{+0.34}_{-0.57}$	$12.45^{+0.18}_{-0.27}$	$46.2^{+1.4}_{-1.9}$	$10.29^{+0.46}_{-0.47}$
56856.91	ACIS/*Chandra*	$\left(6.5^{+1.7}_{-1.4}\right) \times 10^{-2}$	$11.09^{+0.40}_{-0.49}$	$8.71^{+0.20}_{-0.21}$	$31.7^{+1.1}_{-1.0}$	$7.12^{+0.43}_{-0.42}$

NOTE: The X-ray absorbed flux errors are given with a 68% confidence level. Absorbed fluxes from ACIS in the energy range $10-15\,\mathrm{keV}$ are extrapolated values from the spectral model for comparison with the EPIC X-ray absorbed flux value in this energy range.

Table A3. SXP 1062 hardness ratios according to Eq. 1 and using absorbed X-ray fluxes given in Table A2.

	MJD	HR3	HR2	HR1
EPIC/*XMM-Newton*	56606.80	0.42 ± 0.02	0.59 ± 0.01	$0.49^{+0.52}_{-0.01}$
ACIS/*Chandra*	56827.80	0.79 ± 0.01	~ 1	1
ACIS/*Chandra*	56837.49	0.62 ± 0.02	0.87 ± 0.01	~ 1
ACIS/*Chandra*	56846.30	0.58 ± 0.02	0.83 ± 0.01	~ 1
ACIS/*Chandra*	56856.91	0.57 ± 0.02	0.77 ± 0.01	~ 1

NOTE: The uncertainty of HR3 for the first ACIS observation is $\sim 3 \times 10^{-11}$. The flux in the softest energy band $(0.3-1.0\,\mathrm{keV})$ for this observation is almost zero (see Table A2), which could be due to the high absorption column found in that observation (see Table 6).